Materials Today Energy 45 (2024) 101683

Contents lists available at ScienceDirect

Materials Today Energy

journal homepage: www.journals.elsevier.com/materials-today-energy/

Synergistic effects of 1T−2H MoS_2 and laser-reduced graphene Oxide−ZnO scaffold composite catalyst for efficient hydrogen evolution reaction

K.S. Chandrakantha [a, b], Z. Zuo [a, ***], B.N. Chandrashekar [d], A. Amini [c], K.S. Rangappa [e], S. Srikantaswamy [b, **], C. Cheng [a, *]

[a] Department of Materials Science and Engineering, Southern University of Science and Technology, Shenzhen, 518055, China
[b] Center for Materials Science and Technology (CMST), University of Mysore, Karnataka, 570006, India
[c] Center for Infrastructure Engineering, Western Sydney, Kingswood, New South Wales, 2751, Australia
[d] Department of Chemistry, Sri Adichunchanagiri First Grade College, Affiliated to University of Mysore, Channarayapatana, Karnataka, 573116, India
[e] Institution of Excellence, Vijnana Bhavan, University of Mysore, Manasagangotri, Mysore, 570006, India

ARTICLE INFO

Article history:
Received 29 January 2024
Received in revised form
26 August 2024
Accepted 27 August 2024
Available online 31 August 2024

Keywords:
Hydrothermal synthesis
2D materials
Alkaline HER
Water splitting
Energy conversion
Charge transfer

ABSTRACT

A composite catalyst, zinc-doped laser-reduced graphene oxide (LrGO), is synthesized with highly dispersed molybdenum disulfide (MoS_2) nanolayers using laser exfoliation followed by a hydrothermal process. The resultant LrGO−ZnO/1T−2H MoS_2 (GZM3) catalyst exhibits enhanced hydrogen evolution reaction (HER) catalytic performance and improved stability. It achieves small overpotentials of 94 and 191.5 mV at a current density of 10 mA cm^{-2}, under acidic and alkaline conditions, respectively. This superior catalytic activity is attributed to the high electrical conductivity and large electrochemical surface area of graphene, along with efficient charge transfer facilitated by Zn ions between LrGO−ZnO and 1T−2H MoS_2.

1. Introduction

Hydrogen is emerging as a promising and indispensable component in the global pursuit of clean energy. It has the potential to replace fossil fuels, significantly reduce greenhouse gas emissions, and mitigate dependence on non-renewable resources for a sustainable future [1,2]. Electrochemical hydrogen production is one of the most effective methods for advancing sustainable development. However, the environmentally friendly production of hydrogen via water electrolysis is hampered by the slow kinetics of the hydrogen evolution reaction (HER) and the oxygen evolution reaction (OER) [3,4].

Hybrid electrochemical catalysts play a crucial role in overcoming this challenge [5,6]. In fact, large surface area, high porosity, long-term stability, high conductivity, high turnover frequency (TOF) [7], favorable work function (Φ) [8,9], and low Gibbs free energy ($\triangle G_H \sim 0$) [10], are essential characteristics for catalysts involved in water splitting [11,12]. Platinum-based electrocatalysts are considered the most efficient catalysts for HER due to their high catalytic activity and stability [13]. However, the high cost and low abundance of Pt catalysts limit their commercial applications [14,15]. As a result, researchers have been exploring alternative, cost-effective, and non-noble HER catalysts [16].

Recent research has shown the potential of 2H-MoS_2, 1T-MoS_2, and mixed-phase 1T−2H MoS_2 catalysts for green hydrogen production [17−21]. 1T−2H MoS_2 is a promising electrocatalyst due to its intrinsic properties, including abundant active sites and high conductivity [22−26]. To further improve the catalytic performance, researchers have investigated the incorporation of graphene into several composite materials (Table S2). Owing to Its outstanding properties, such as its large surface area, excellent conductivity, and easy functionalization, graphene an excellent

* Corresponding author.
** Corresponding author.
*** Corresponding author.
E-mail addresses: 12012513@mail.sustech.edu.cn (Z. Zuo), srikantaswamy@envsci.uni-mysore.ac.in (S. Srikantaswamy), chengc@sustech.edu.cn (C. Cheng).

https://doi.org/10.1016/j.mtener.2024.101683

choice for electrochemical applications [27]. The resulting 1T−2H MoS_2/graphene composite leverages the synergistic effects of both components [28] and provides a platform for improved water splitting. Moreover, the incorporation of transition metal atoms into this composite electrocatalyst offers the potential to modulate its electronic properties and create new active sites, thereby optimizing catalytic activity [29,30]. Overall, the development of efficient and stable catalysts for water splitting at high current densities is crucial for the practical production of green hydrogen and for improving the physicochemical performance of electrocatalysis [31].

This work prepared a novel Zn^{2+} ion-mediated mixed-phase LrGO−ZnO/1T−2H MoS_2 composite with high-conductive linkers that effectively function as charge transfer channels. The generation of 1T−2H MoS_2 nanolayers on the LrGO−ZnO surface led to the formation of additional edges with active sites, and significantly improved HER activity compared to pure MoS_2, Zn−MoS_2, and LrGO-MoS_2 catalysts. It was demonstrated that only 94 and 191.5 mV were required to achieve the current density of 10 mA cm^{-2} under acidic and alkaline conditions, respectively. The improved electrocatalytic performance of the catalyst is due to the combined effects of 1T−2H MoS_2, the high conductivity of the LrGO surface, and the presence of ZnO nanoparticles. This research proposes a strategy for the development and synthesis of low-cost, high-performance catalysts for hydrogen production.

2. Experimental section

2.1. Materials and chemicals

The following materials were used including graphene oxide (GO) powder (Soochow Hengqiu Graphene Technology (Suzhou) Co., Ltd.), sodium hydroxide (NaOH, Aladdin Chemical Reagent Co., Ltd.), ammonium molybdate tetrahydrate ($(NH_4)_6Mo_7O_{24}\cdot 4H_2O$, Aladdin Chemical Reagent Co., Ltd.), and thiourea ($RC(S)NR_2$, Aladdin Chemical Reagent Co., Ltd.), zinc chloride ($ZnCl_2$, Sigma-Aldrich) and platinum on carbon (Pt/C, Sigma-Aldrich), Ultrapure water with a resistivity of 18.25 MΩ cm was attained from a Millipore system. 5 wt% of Nafion® solution was purchased from Alfa Aiser.

2.2. Synthesis of LrGO−ZnO/1T−2H MoS_2 composites

To synthesize the LrGO−ZnO/1T−2H MoS_2 composite, 0.05 g of four variants of LrGO−ZnO powder were separately mixed with 3.250 g of ammonium molybdate tetrahydrate $(NH_4)_6Mo_7O_{24}\cdot 4H_2O$ and 3.175 g of thiourea in 100 ml of deionized water. The resultant mixture was transferred to a Teflon-lined autoclave and heated at 220 °C for 16 h. After the reaction, the product was centrifuged and washed multiple times with deionized water and ethanol. Finally, the obtained solution was freeze-dried for about 24 h to obtain the LrGO−ZnO/1T−2H MoS_2 composite. The schematic diagram of the synthesis process is shown in Fig. S1, and the procedures for the preparation of LrGO [32], LrGO−ZnO, Zn−MoS_2, and MoS_2 are described in ESI*.

2.3. Characterizations

X-ray photoelectron spectroscopy (XPS) measurements were carried out on a Thermo Scientific ESCALAB 250 X-ray photoelectron spectrometer equipped with a monochromatic Al Kα X-ray source (1486.6 eV). X-ray diffraction (XRD) patterns were obtained using a Rigaku SmartLab X-ray diffractometer. The Raman spectra were acquired from a Horiba Jobin Yvon LabRAM HR spectrometer equipped with a 532 nm laser. The surface morphologies of the composite samples were investigated by scanning electron microscopy (SEM) using a Hitachi SU8010 scanning electron microscope. Transmission electron microscopy (TEM) images were taken from a Tecnai G2 F20 S-TWIN microscope operating at 200 kV. Kratos AXIS Supra-Spectrometer, Ultraviolet Photoelectron Spectroscopy (UPS), is used to study the work function and fermi energy level, where He I radiation (21.22 eV) was used as the photon source.

2.3.1. Electrochemical measurements

The electrochemical measurements were conducted using a CH-instrument (660E) electrochemical workstation in a three-electrode system. The acidic electrolyte was a 0.5 M H_2SO_4 solution, whereas 1 M KOH solution was used to prepare an alkaline solution. All the electrolytes were primarily processed using nitrogen with high purity. The glassy carbon electrodes (GCE) coated with as-prepared composite samples served as working electrodes, while the Ag/AgCl electrode and graphite electrode worked as the reference and counter electrodes, respectively. Linear sweep voltammetry (LSV) tests were conducted in 0.5 M H_2SO_4 and 1 M KOH solutions at a potential scan rate of 5 mV s^{-1}; this was performed after the 300th cycle of cyclic voltammetry (CV) tests to stabilize the current. The 24-h amperometric current−time (IT) response was measured using a chronoamperometry technique. The electrochemical impedance spectroscopy (EIS) was recorded within the frequency range of 0.1−100 kHz at an overpotential of 180 mV and an AC interrupt voltage of 5 mV. The potentials reported in this study were referred to as the reversible hydrogen electrode (RHE) by converting the Ag/AgCl electrode potential to the RHE using the following equation: $E_{RHE} = E_{0(Ag/AgCl)} + E_{(Ag/AgCl)} + 0.059 \times pH$. $E_{0(Ag/AgCl)}$ was taken as 0.210 V at pH 0.3 and pH 13, and $E_{(Ag/AgCl)}$ was the working voltage in the measurements.

2.3.2. Density functional theory (DFT) calculation

Periodic DFT calculations were conducted using the Vienna Ab initio simulation package by employing a plane-wave basis set and the projector augmented-wave method. The exchange-correlation functional with the Perdew−Burke−Ernzerhof format was selected within the generalized gradient approximation while incorporating van der Waals corrections (optPBEvdW). To verify the impact of van der Waals corrections, calculations were additionally performed without these corrections (Table S3). The energy cutoff for the plane-wave basis set was set to 400 eV. To eliminate spurious dipole interactions between periodic images, dipole corrections were implemented. During the simulation, a portion of the system was relaxed until the forces reached a magnitude of <0.01 eV $Å^{-1}$ on each atom. For structural optimization, a $6 \times 6 \times 1$ k-point mesh was used, while a $9 \times 9 \times 1$ k-point mesh was used for the energy and electronic structure calculations. To mitigate interactions between neighboring slabs, a vacuum region exceeding 20 Å was incorporated.

3. Results and discussion

3.1. Morphology, structure, and composition characterizations

The LrGO−ZnO/1T−2H MoS_2 (GZM3) catalyst exhibited the highest electrocatalytic activity among the synthesized catalysts (Figs. S8a and S8b). Due to its superior performance, it was selected for comprehensive characterization and subsequent evaluation of the hydrogen evolution reaction (HER). The morphology, structure and composition of the catalyst were determined using TEM, HRTEM and SAED pattern analysis, which are advanced techniques for characterizing nanoscale materials. The LrGO−ZnO/1T−2H MoS_2 (GZM3) catalyst was first characterized by TEM with EDS (Fig. 1). Fig. 1a shows the typical composite morphology, in which a

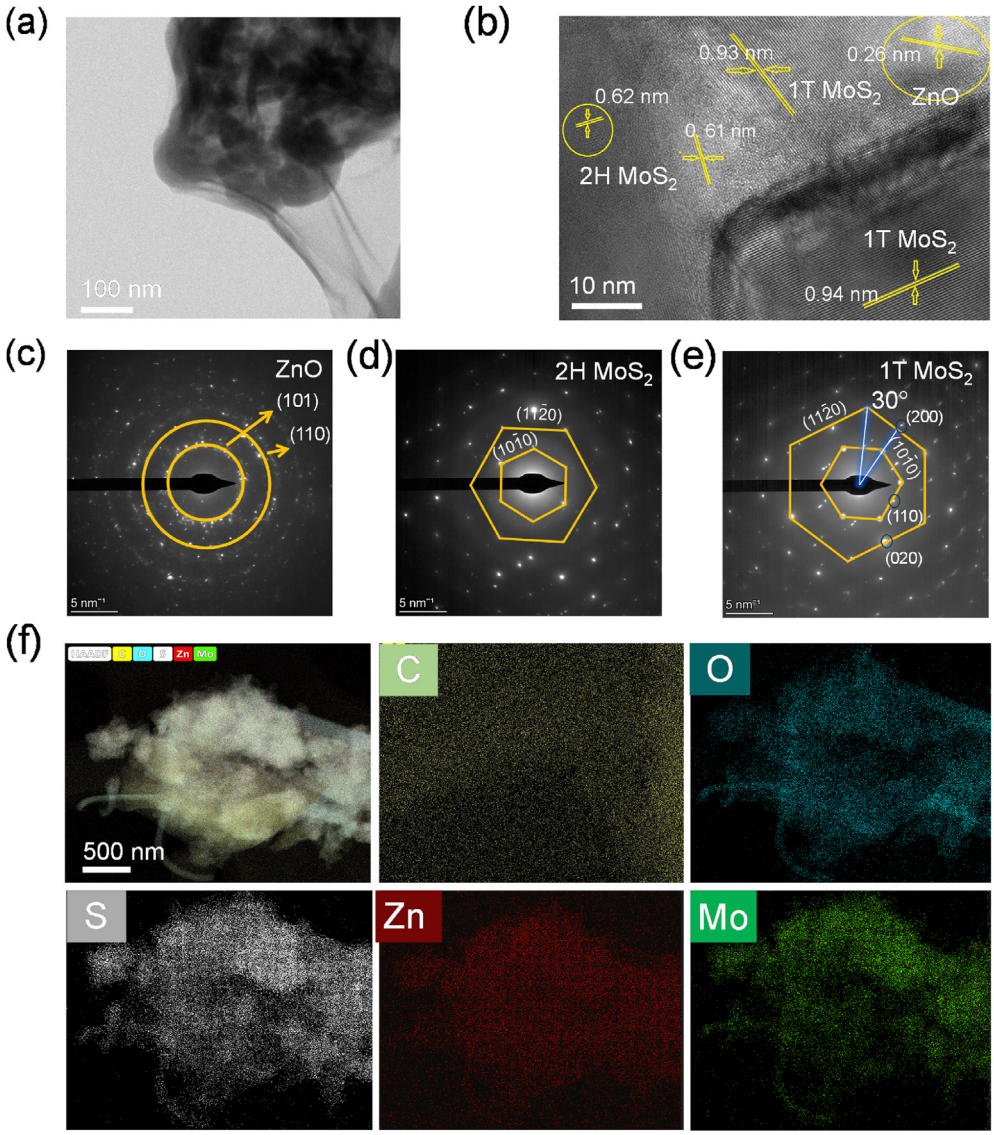

Fig. 1. (a) TEM images show a thin layer of graphene around the composite. (b) HRTEM images of LrGO–ZnO/1T–2H MoS_2 (GZM3); (c–e) SAED pattern of (c) ZnO; (d) 2H MoS_2; and (e) 1T MoS_2. (f) TEM elemental analysis of LrGO–ZnO/1T–2H MoS_2 (GZM3), High-Angle Annular Dark-Field (HAADF) EDX imaging reveals the spatial distribution of C, O, S, Zn, and Mo elements in the GZM3 catalyst.

thin layer of graphene appears to surround the composite. HRTEM imaging provides an atomic-scale perspective and reveals the crystalline structure of the composite. The HRTEM image in Fig. 1b highlights the detailed spatial arrangement of the 1T–2H MoS_2 phases on the LrGO–ZnO surface, as well as the coexistence of ZnO, 2H-MoS_2, and 1T-MoS_2 phases within the material. This analysis was confirmed by the measured interplanar distances of 0.26 nm (ZnO), 0.61–0.63 nm (2H-MoS_2), and 0.93–0.94 nm (1T-MoS_2). The SAED patterns acquired along the [001] zone axis provided further structural insights. The SAED pattern for the GZM3 composite showed clear diffraction spots (hkl) with indices (101) and (110). These indices are consistent with the hexagonal wurtzite structure of the typical ZnO phase, as shown in Fig. 1c. The SAED patterns of 2H-MoS_2 and 1T-MoS_2 (Fig. 1d and e) within the composite provide important insights into their structural differences. The 2H-MoS_2 phase exhibits a hexagonal lattice structure with trigonal-prismatic coordination, as evidenced by the key diffraction points (hk-l) indexed as (11–10) and (11–20). These points show the stable and uniform crystal structure of 2H-MoS_2 corresponding to the in-plane directions, trigonal symmetry, and interlayer interactions. In contrast, the 1T MoS_2 phase exhibits more complex octahedral coordination, where each Mo atom is coordinated by six S atoms vin a different atomic arrangement. The SAED pattern for 1T-MoS_2 includes diffraction points with indexes (11–10) and (11–20) and additional points at 30° intervals indexed as (110), (200) and (020). These spots indicate the structural alignment and symmetrical variations inherent in the octahedral arrangement [33]. Additionally, the element mapping shown in Fig. 1f provides a visual representation of the distribution of elements within the composite. The mapping shows that carbon (C), oxygen (O), sulfur (S), zinc (Zn), and molybdenum (Mo) are evenly distributed throughout the material. This uniform distribution confirms the successful integration of these elements into the GZM3 catalyst, which is critical to ensuring consistent material properties and performance across the GZM3 catalyst.

X-ray photoelectron spectroscopy (XPS) analysis is conducted to study the chemical compositions and valence states of the LrGO–ZnO/1T–2H MoS_2 (GZM3) composite. The survey scan

(Fig. 2a) confirms the presence of O, C, S, Zn, and Mo elements in the composite [34]. The peaks corresponding to Mo−S, O−C, and H−O−C are observed at binding energies of 530.90 eV, 531.71 eV, and 530.53 eV (Fig. 2b), which originated from oxygen vacancies in the composite. These oxygen vacancies, coupled with the surface defects of LrGO, provide sufficient bridging sites for Zn. Two deconvoluted C1s spectra located at 284.823 eV corresponded to sp^2 hybridized carbon (Fig. 2c) and were corroborated by FTIR data (Fig. S2), and 286.26 eV represents the plasmon loss features [35]; this observation further confirms the presence of LrGO in the composite. The illustration Fig. 2d demonstrates the existence of ZnO along with Zn ions, as evidenced by the Zn $2p_{3/2}$ peak at 1023.1 eV and the Zn $2p_{1/2}$ peak at 1046.22 eV. The deconvoluted Mo 3d peaks (Fig. 2e) exhibit six peaks: Mo $3d_{5/2}$ at 228.69 eV and Mo $3d_{3/2}$ at 232.07 eV correspond to the 1T phase of MoS_2, while Mo $3d_{5/2}$ at 229.69 eV and Mo $3d_{3/2}$ at 233.23 eV correspond to the 2H phase of MoS_2 [36]. The peak observed for S 2s at 226.11 eV spectra (Fig. 2e) corresponded to the terminal bridging and apical S^{2-} state [36], verifying the existence of 1T−2H MoS_2 in the composite. In Fig. 2f, the S2p peaks at 162.44 eV, and the oxidized sulfur defects are observed at 168.7 eV; these results substantiate the S defects and uniform distribution of 1T−2H MoS_2 on the surface of LrGO−ZnO. These contributed to the formation of the geometric and electronic structure of 1T−2H MoS_2, exerting a direct influence on the electrocatalytic performance [28]. To observe the structural phase changes in the composite before hydrothermal synthesis of the composite, XPS analysis of LrGO−ZnO and MoS_2 are provided in ESI* (Fig. S3) (a) Cs 1s, (b) O 1s, and (c) Zn $2p_3$, as well as XPS analyses of MoS_2 for (d) S 2p and (e) Mo 3d.

X-ray diffraction (XRD) analysis confirmed the successful synthesis of the LrGO−ZnO/1T−2H MoS_2 composite and showed the coexistence of multiple phases, including 1T and 2H MoS_2, ZnO, and possible Zn−Mo−S interactions. The identified peaks provided important insights into the structural properties of the composite. In Fig. 3a, the peaks at 9.4° and 14.2°, corresponding to the (002) planes of the 1T and 2H phases of MoS_2, respectively, confirmed the presence of both structural variants in the composite and are consistent with the JCPDS card numbers 37-1492 and 77-171 for 2H and 1T MoS_2, respectively. The calculated d-spacings of 0.94 nm for 1T MoS_2 and 0.62 nm for 2H MoS_2 correlate with the results of HRTEM (Fig. 1b) and support the successful incorporation of both phases. Additional peaks at 15.2°, 18.4°, 36.2°, and 50° represent the hkl values of (002), (004), (102), and (200) and indicate the hexagonal phase of MoS_2 on the LrGO surface. The clear peak at 56.2° (105) further supports the identification of MoS_2 within the composite, indicating sulfur vacancies in 1T−2H-MoS_2 phase. The analysis confirmed the presence of ZnO in the composite, as evidenced by characteristic peaks at 31.8° (100) and 34° (101) with a d-spacing of 0.26 nm, corresponding to JCPDS card number 89-1397 matches. The clear peak at 58.9° (110) indicates the possible formation of a Zn−Mo−S phase, which likely results from interactions between Zn and MoS_2 during synthesis and could improve the performance of the composite in catalytic applications. The integration of LrGO, ZnO, and 1T−2H MoS_2 into a single structure offers promising potential for various applications, especially in energy conversion catalysis. The GO and LrGO XRD patterns shown in Fig. S4 provide additional support for the structure description.

Raman spectroscopy is used to investigate the chemical composition of the composite catalyst. Both rGO and LrGO showed characteristic G and D bands in their Raman spectra (Fig. S5a). The ratio of D-band and G-band intensities (I_D/I_G) can reflect the number of layers present in the graphene oxide material as well as the distance between defects in the graphene lattice [37,38]. The I_D/I_G ratio increases from 0.84 for GO to 0.85 for LrGO (Fig. S5a), indicating increased disorders such as defects and pores in LrGO [27,29]. This can be attributed to the elimination of oxygen functional groups and the formation of oxygen defects on the surface of graphene [39]. The slight shift of the G-band to higher energy confirms the covalent grafting of organic molecules that isolated sp^2 carbon atoms. Raman spectroscopy confirmed the presence of graphene layers in LrGO−ZnO/1T−2H MoS_2 with characteristic peaks between 300 and 1650 cm^{-1} (Fig. S5b). The strong overlap of the 1T−2H MoS_2 phase with the LrGO surface was evident. Detailed analysis of the 340−440 cm^{-1} region (Fig. 3b) revealed vibrational modes assigned to E1g, E12g, and A1g by comparison with LrGO-MoS_2, Zn−MoS_2, and MoS_2 spectra. The differences between these

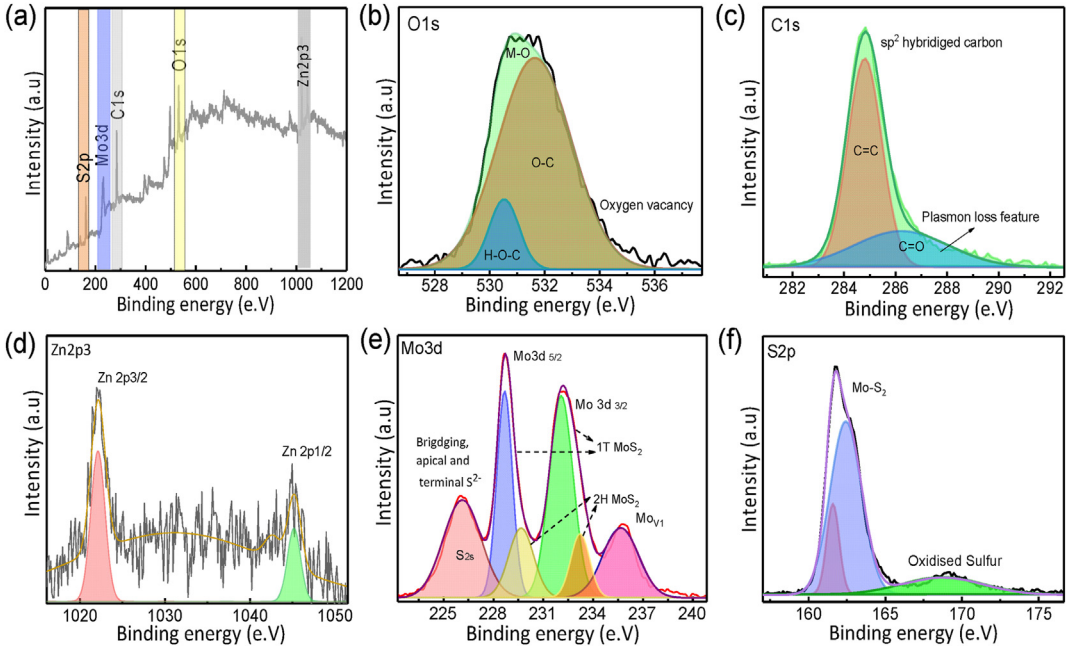

Fig. 2. (a) Full XPS spectrum of LrGO−ZnO/1T−2H MoS_2 heterostructure and peak deconvolution of (b) O 1s, (c) C 1s, (d) Zn 2p3, (e) Mo 3d spectra, and (f) S 2p.

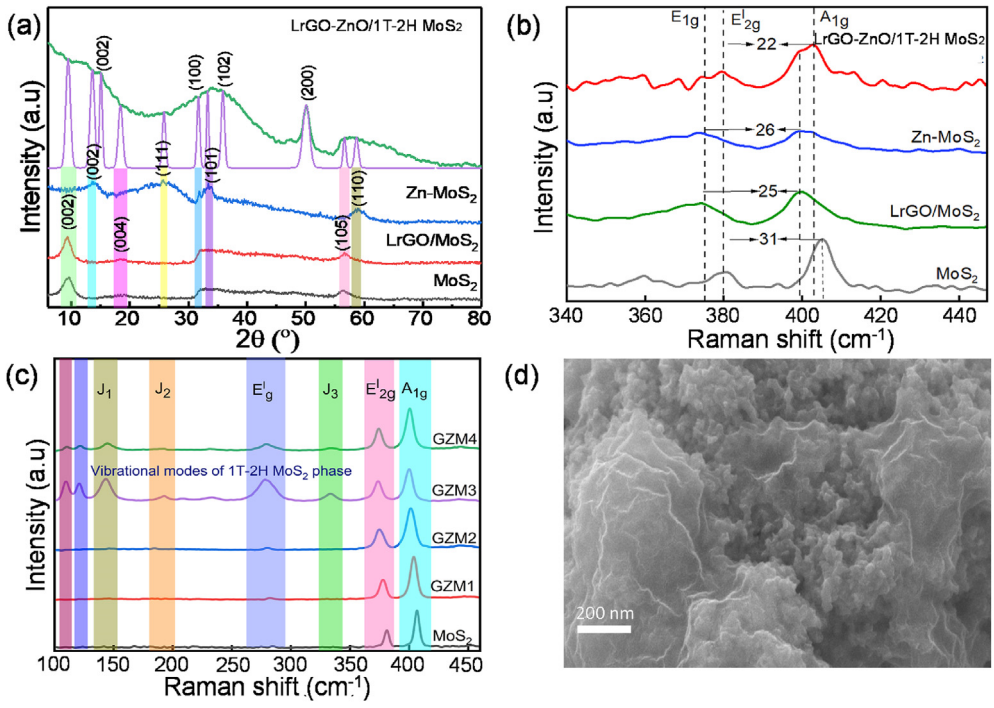

Fig. 3. (a) XRD patterns of MoS_2, LrGO-MoS_2, Zn−MoS_2, and LrGO−ZnO/1T−2H MoS_2 (GZM3). (b) Raman spectra in the range of 340−440 cm^{-1} of the E^1_g, E^1_{2g}, and A^1_g peaks of MoS_2, LrGO-MoS_2, Zn−MoS_2, and LrGO−ZnO/1T−2H MoS_2 (GZM3). (c) Raman spectra in the range of 100−450 cm^{-1} of J_1, J_2, J_3, E^1_g, E^1_{2g}, and A^1_g peaks of MoS_2, LrGO−ZnO/1T−2H MoS_2 (GZM3) in comparison with LrGO−ZnO/1T−2H MoS_2 (GZM4), LrGO-ZnO/MoS_2 (GZM1), and LrGO-ZnO/MoS_2 (GZM2). (d) FE-SEM micrograph of LrGO−ZnO/1T−2H MoS_2 (GZM3).

characteristic peaks confirm the formation of the mixed phase of 1T−2H MoS_2, as well as the 2D atomic arrangements within the catalyst structure. A^1g corresponds to out-of-plane vibrations of S atoms, and frequency shifts of A^1g and E^12g are observed as a function of the number of layers. A smaller difference between these peaks indicates a more disordered structural nature of LrGO−ZnO/1T−2H MoS_2. The A^1g/E^12g intensity ratio of LrGO−ZnO/1T−2H MoS_2 is 1.06 cm^{-1}, suggests the monolayer-dependent properties of the catalyst. The Raman shift in the range of 100−450 cm^{-1} (Fig. 3c) shows the characteristic peaks J1, J2, J3, E^1g, E^12g, and A^1g. When comparing LrGO−ZnO/1T−2H MoS_2 (GZM3) with LrGO−ZnO/1T−2H MoS_2 (GZM4), LrGO-ZnO/MoS_2 (GZM2), LrGO-ZnO/MoS_2 (GZM1), and MoS_2, it is clear that the GZM3 and GZM4 composite materials exhibit specific vibrational properties of 1T−2H1T−2H MoS_2 that reflect the complex interaction of these components.

The FE-SEM image in Fig. 3d provides a detailed analysis of the LrGO−ZnO/1T−2H-MoS_2 composite's microstructure and illustrates the arrangement of the MoS_2 layers within the LrGO−ZnO matrix. The SEM images in Fig. S6 provide insights into the morphological difference between graphene oxide and laser-reduced graphene oxide. The morphological properties before the electrochemical reaction are shown in Fig. S7. Further details can be found in the ESI.

3.2. Electrochemical HER characterization

To assess the catalytic performance in both acidic and alkaline environments, we perform the electrochemical characterizations on the electrodes for HER using a three-electrode system in 0.5 M H_2SO_4 and 1 M KOH electrolytes at room temperature. The polarization curves show that LrGO−ZnO/1T−2H MoS_2 is still inferior to Pt/C in terms of overpotentials. Also, it exhibits an outstanding catalytic activity, which only needs 94 and 191.5 mV to deliver the current density of 10 mA cm^{-2} under acidic and alkaline conditions, respectively, better than those of LrGO/MoS_2 (150 and 234.9 mV), Zn/MoS_2 (155 and 282.2 mV), and MoS_2 (226 and 376 mV) (Figs. 4a, 5a, and Table S1). In addition, LrGO−ZnO/1T−2H MoS_2 possesses low Tafel slopes of 41.17 and 58 mV dec^{-1} in acidic and alkaline environments, lower than LrGO/MoS_2 (43.74 and 75.75 mV dec^{-1}), Zn/MoS_2 (54.84 and 87.97 mV dec^{-1}), and MoS_2 (66 and 100 mV dec^{-1}) (Figs. 4b and 5b and Table S1). Compared to other controlled catalysts, this fact determines a more favorable Volmer-Heyrovsky mechanism for LrGO−ZnO/1T−2H MoS_2. The comparison results of MoS_2-based catalysts are tabulated in Table S2. Fig. S8a and S8b show the linear sweep voltammetry (LSV) curves of catalysts doped with varying Zn content (1−4 wt%) and correlate their Tafel slopes with the activity of the hydrogen evolution reaction (HER) in both acidic (0.5 M H_2SO_4) and alkaline (1 M KOH) environments. The optimized LrGO−ZnO/1T−2H MoS_2 (GZM3) is characterized by its superior HER kinetics, which is reflected in its lower Tafel slope.

The electrochemical impedance spectroscopy (EIS) test is adopted to analyze the charge transfer kinetics of electrodes. In acid and alkaline electrolytes, the Nyquist plot of LrGO−ZnO/1T−2H MoS_2 shows the smallest charge transfer resistance (Rct) of 6 Ω and 10 Ω, respectively, apparently smaller than those for LrGO/MoS_2, Zn/MoS_2, and MoS_2 (Figs. 4c and 5c). Such low resistance values illustrate the fast charge transfer kinetics of LrGO−ZnO/1T−2H MoS_2. To further probe the electrocatalytic behaviors of LrGO−ZnO/1T−2H MoS_2 composite electrode, the electrochemical surface area (ECSA) is measured based on double-layer capacitance (C_{dl}) through cyclic voltammetry (CV) tests. The C_{dl} values of LrGO−ZnO/1T−2H MoS_2 under acid and alkaline (Figs. 4d and 5d) conditions are 103.19 and 56.35 mF cm^{-2}, respectively, much larger than those of LrGO/

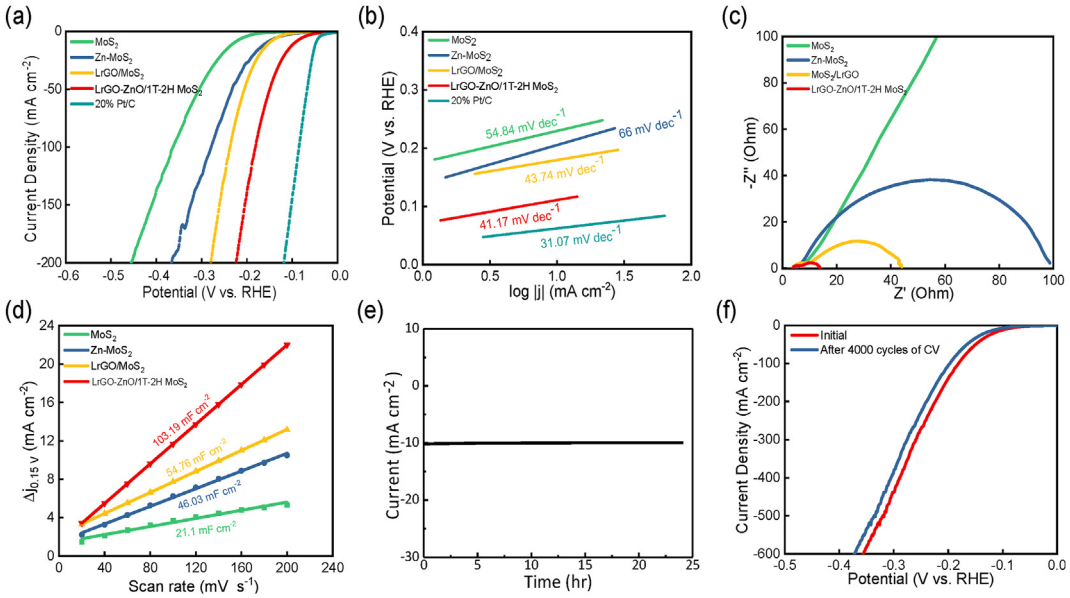

Fig. 4. Hydrogen evolution reaction in 0.5 M H_2SO_4. (a) LSV curves, (b) Tafel slopes, (c) EIS curves, (d) C_{dl} values of different electrodes, (e) Amperometry current–time (IT) response of the LrGO–ZnO/1T–2H MoS_2 electrode at a constant current density of 10 mA cm^{-2}, (f) LSV curves of LrGO–ZnO/1T–2H MoS_2 before and after 4000 cycles of CV.

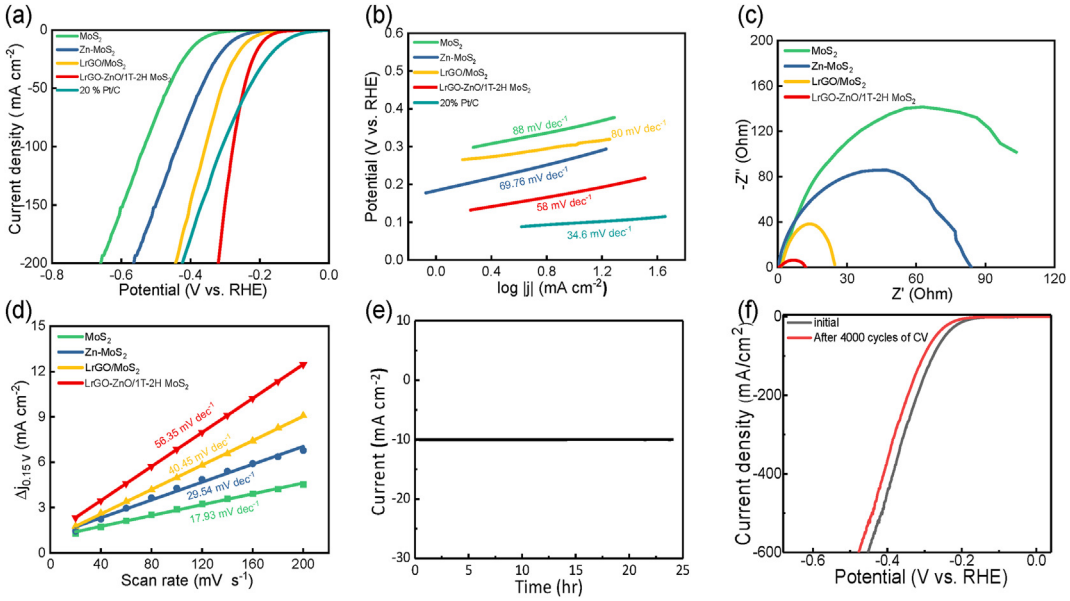

Fig. 5. Hydrogen evolution reaction in 1 M KOH. (a) LSV curves, (b) Tafel slopes, (c) EIS curves, (d) C_{dl} values of different electrodes, (e) Amperometry current–time (IT) response of the LrGO–ZnO/1T–2H MoS_2 electrode at the constant current density of 10 mA cm^{-2}, (f) LSV curves of LrGO–ZnO/1T-2H MoS_2 before and after 4000 cycles of CV.

MoS_2 (54.76 and 40.45 mF cm^{-2}), Zn/MoS_2 (46.03 and 29.54 mF cm^{-2}), and MoS_2 (21.1 and 17.93 mF cm^{-2}); This observation proves more abundant active sites of LrGO–ZnO/1T–2H MoS_2 for catalytic reactions.

The electrochemical endurance of composite electrodes is a critical factor in determining their potential industrial uses. The amperometry current–time (IT) response in Figs. 4e and 5e depicts that LrGO–ZnO/1T–2H MoS_2 works stably at 10 mA cm^{-2} for 24 h in both acidic and alkaline environments [6]. In Figs. 4f and 5f, the LSV was determined before and after 4000 CV cycles, which shows the least deterioration in catalytic performance in both acidic and alkaline conditions. The excellent operational stability of LrGO–ZnO/1T–2H MoS_2 is attributed to its preserved structural and compositional integrity, as confirmed by post-electrochemical SEM, TEM, and XRD analyses (Fig. S9). This reveals its prominent stability under practical current conditions and offers promising alternatives for future applications. Overall, the LrGO–ZnO/1T–2H MoS_2 catalyst presents enhanced electrocatalytic performance.

To further elucidate the catalytic efficiency, turnover frequency (TOF) analysis was conducted to quantify the hydrogen generation rate per active site. The results show a strong correlation between increased electrochemical surface area (ECSA) and turnover frequency (TOF), with TOF values of 2.62 s^{-1} and 2.95 s^{-1} for hydrogen production per active site at an overpotential of 150 mV in acidic and alkaline media, respectively (Fig. 6a). Further investigations

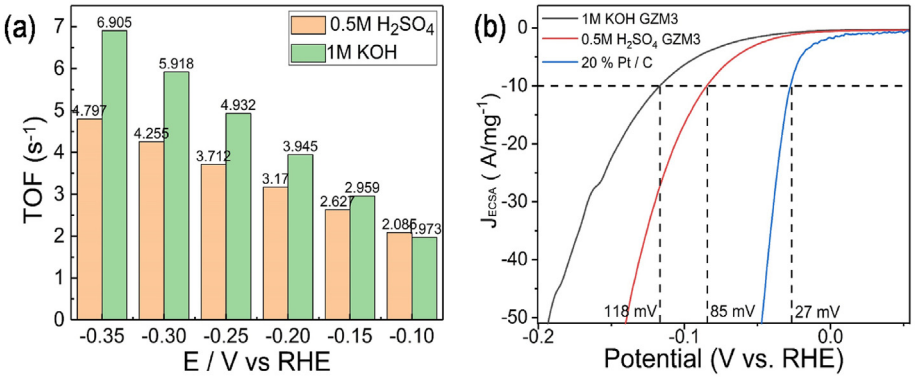

Fig. 6. (a) TOF values at different potentials for GZM3 in acidic and alkaline conditions; (b) Specific catalytic activity in 0.5 M H_2SO_4 and 1 M KOH.

address the interplay between electrochemical surface area (ECSA) and charge transfer as well as the loading mass in different variants of LrGO−ZnO/1T−2H MoS_2 catalyst electrodes, with a particular focus on their effectiveness in driving the hydrogen evolution reaction (HER). It is observed that the ECSA, which is positively correlated with the loading mass of the catalyst (0.217 mg cm^{-2}), shows a pronounced increase in LrGO−ZnO/1T−2H MoS_2 HER activity in two different electrolytes. ECSA normalizes the observed current density, revealing a specific activity at an overpotential of 85 mV and 118 mV at 10 A mg^{-1} (Fig. 6b). This fact suggests an increase in catalytic efficiency beyond the improvement provided by ECSA alone. The variables that contributed to the improved catalytic activity are crucial. The significant 1T−2H-MoS_2 phase content in the GZM3 catalyst is primarily responsible for its outstanding performance. To quantify this phase, we integrated the area of Raman spectral peaks associated with the 1T−2H phase (Fig. 3c) and represented the results as a percentage distribution in Fig. S10a. Our analysis indicates a direct correlation between Zn concentration and the 1T−2H phase ratio, with GZM3 (3% Zn) possessing the highest proportion of this phase (52.71%). These findings corroborate the successful synthesis of the LrGO−ZnO/1T−2H MoS_2 composite, highlighting the influence of Zn concentration on phase composition. Additionally, the study evaluated mass activity, a crucial indicator of electrocatalyst performance. This parameter, representing the current normalized by catalyst loading, was found to be 2 A mg^{-1} and 2.98 A mg^{-1} at 150 mV in acidic and alkaline conditions, respectively (Fig. S10b). These results highlight the superior catalytic performance of LrGO−ZnO/1T−2H MoS_2 (Note S1).

3.2.1. Charge transfer mechanism

The charge transfer mechanism in the LrGO−ZnO/1T−2H MoS_2 composite is mainly influenced by its work function and Fermi levels, which determine the efficiency of electron transfer during electrochemical reactions. The work function is the minimum amount of energy required to remove an electron from the surface of a material into a vacuum. It is a crucial property that influences how easily electrons can be transferred between an electrode and electrolyte during electrochemical processes [40,41]. By using ultraviolet photoelectron spectroscopy (UPS), as shown in Fig. 7a, the work function of LrGO−ZnO/1T−2H MoS_2 is determined to be 4.41 eV using the formula $\phi = h\nu - E_{cut\text{-}off}$. This relatively moderate work function enables efficient charge transfer at the composite interfaces. The Fermi energy level of the catalyst was calculated to be −0.09 eV by using the formula $EF = \phi - E_o$ (Fig. 7a), and this value was compared to those of the individual components of the catalyst, such as MoS_2 (ϕ = 4.04 eV, EF = −0.46) [8], graphene (ϕ = 4.4 eV, E_F = −0.1) [9,42], and ZnO (ϕ = 4.7 eV, E_F = 0.2) [43]. Fig. 7b illustrates the work functions and Fermi levels of graphene, ZnO, and 1T−2H MoS_2, highlighting the potential for efficient electron transfer through Zn^{2+} ions. The close proximity of these Fermi levels highlights the potential for efficient electron movement between components, especially when the Fermi levels are properly aligned. The presence of Zn^{2+} ions within the composite significantly enhances electron transport by creating conduction pathways and mediating charge transfer during electrocatalysis. The strong potential for charge transfer within the LrGO−ZnO/1T−2H MoS_2 composite suggests that strategically manipulating the potential could further optimize these electron transport

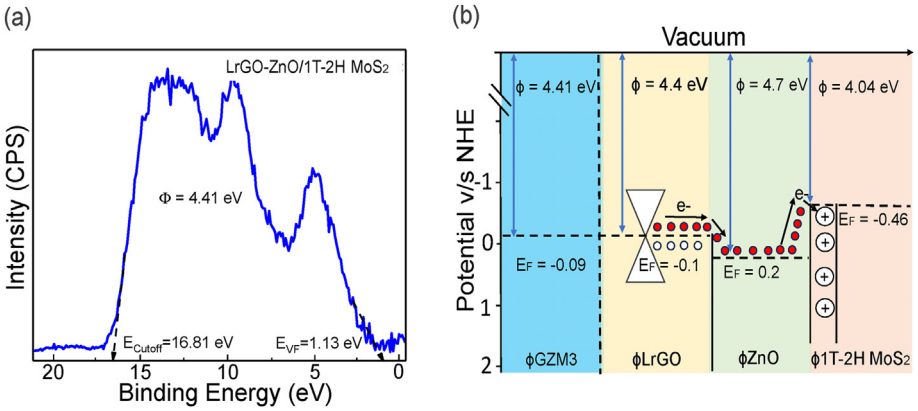

Fig. 7. (a) UPS spectra of LrGO−ZnO/1T−2H MoS_2 (GZM3); (b) schematic energy band diagrams illustrating the electron transfer pathway within the LrGO−ZnO/1T−2H MoS_2 (GZM3) composite electrode.

pathways. By tuning electron density and enhancing component interactions, the composite could achieve significant improvements in electrocatalytic activity and energy conversion efficiency (Notes S2, S3).

3.2.2. Density functional theory (DFT) calculation

To understand the mechanism behind the enhanced catalytic performance of LrGO-ZnO/MoS_2, density functional theory (DFT) calculations were carried out, as shown in Fig. S11, and the determined Gibbs free energies are tabulated in Table S3. A crucial parameter in evaluating the thermodynamic feasibility of electrochemical reactions is the free energy of hydrogen adsorption, denoted as ΔG_H^* [10,44]. Negative values of ΔG_H^* indicate that a reaction is both favorable and spontaneous when it comes to the hydrogen evolution reaction (HER) (Note S4). Conversely, values close to zero are preferred as they represent optimal catalytic performance. The calculated ΔG_H^* for LrGO/MoS_2 is −0.593 eV, while for the LrGO-ZnO/MoS_2 composite, it is −0.280 eV, as shown in Fig. S11f. These results suggest that spontaneous responses occur with both electrode configurations. However, the introduction of metal ions, especially Zn^{2+}, increases the intrinsic catalytic activity. The Zn^{2+} ions serve as a bridge and enable rapid charge transfer from the graphene component to the catalytically active MoS_2 layer. This mechanism effectively promotes the reduction of edge-adsorbed hydrogen species (denoted as H*) and their subsequent conversion to molecular hydrogen (H_2).

4. Conclusions

In this work, we report a practical strategy to synthesize LrGO−ZnO/1T−2H MoS_2 as a composite electrode for electrocatalytic hydrogen evolution reactions (HER). Our findings highlight the potential of using bridging agents to enhance charge transfer between the substrate and the nanosheets. The combination of the unique properties of each component in the composite electrode leads to a significant improvement in both HER activity and stability. The LrGO−ZnO/1T−2H MoS_2 electrode demonstrates low overpotentials of 94 mV and 191.5 mV at 10 mA cm^{-2} under acidic and alkaline conditions, respectively, with turnover frequencies (TOFs) of 2.62 s^{-1} and 2.95 s^{-1}, confirming its HER performance. In both acidic and alkaline electrolytes, the electrode exhibits stable operation for 24 h, with minimal degradation in catalytic capabilities. These findings are valuable for developing efficient and stable electrocatalysts for HER across a wide pH range.

Funding information

The authors acknowledge the financial support received from the Shenzhen Science and Technology Program (Grant No. 20231115112954001), the Student Innovation Training Program (Grant No. 2023X01, 2023X02, 2023X03, 2023S03, 2024S21, 2024X31, and 2024X46) from the Southern University of Science and Technology (SUSTech), China. as well as the Special Funds for the Cultivation of Guangdong College Students' Scientific and Technological Innovation (Grant No. pdjh2024c10910, pdjh20242024c10912). SEM and TEM images of this study were obtained using equipment provided by Southern University of Science and Technology Core Research Facilities. The Council of Scientific and Industrial Research (CSIR), HRDG, is acknowledged for the SRF-Direct Grant (124-1660-308/2K23/1), Ministry of Science and Technology, Government of India.

CRediT authorship contribution statement

K.S. Chandrakantha: Writing − review & editing, Writing − original draft, Visualization, Validation, Software, Methodology, Formal analysis, Data curation, Conceptualization. **Z. Zuo:** Writing − review & editing, Data curation. **B.N. Chandrashekar:** Writing − review & editing, Supervision, Data curation, Conceptualization. **A. Amini:** Validation, Project administration. **K.S. Rangappa:** Visualization, Resources, Project administration. **S. Srikantaswamy:** Writing − review & editing, Visualization, Validation, Supervision, Conceptualization. **C. Cheng:** Writing − review & editing, Visualization, Validation, Supervision, Project administration, Funding acquisition.

Declaration of competing interest

The authors declare that they have no known competing financial interests or personal relationships that could have appeared to influence the work reported in this paper.

Data availability

Data will be made available on request.

Appendix A. Supplementary data

Supplementary data to this article can be found online at https://doi.org/10.1016/j.mtener.2024.101683.

References

[1] P.J. Megía, A.J. Vizcaíno, J.A. Calles, A. Carrero, Hydrogen production technologies: from fossil fuels toward renewable sources. A mini review, Energy Fuels 35 (20) (2021) 16403−16415, https://doi.org/10.1021/acs.energyfuels.1c02501.
[2] S. van Renssen, The hydrogen solution? Nat. Clim. Chang. 10 (9) (2020) 799−801, https://doi.org/10.1038/s41558-020-0891-0.
[3] C. Durante, Efficient oxygen evolution reaction electrocatalysts can boost green hydrogen electrosynthesis, Chem Catal. 2 (5) (2022) 923−925, https://doi.org/10.1016/j.checat.2022.04.004.
[4] T. Tang, Z. Duan, D. Baimanov, X. Bai, X. Liu, L. Wang, Z. Wang, J. Guan, Synergy between isolated Fe and Co sites accelerates oxygen evolution, Nano Res. 16 (2) (2023) 2218−2223, https://doi.org/10.1007/s12274-022-5001-3.
[5] C.C.L. McCrory, S. Jung, I.M. Ferrer, S.M. Chatman, J.C. Peters, T.F. Jaramillo, Benchmarking hydrogen evolving reaction and oxygen evolving reaction electrocatalysts for solar water splitting devices, J. Am. Chem. Soc. 137 (13) (2015) 4347−4357, https://doi.org/10.1021/ja510442p.
[6] S. Wang, A. Lu, C.-J. Zhong, Hydrogen production from water electrolysis: role of catalysts, Nano Converg. 8 (1) (2021) 4, https://doi.org/10.1186/s40580-021-00254-x.
[7] S. Anantharaj, P.E. Karthik, S. Noda, The significance of properly reporting turnover frequency in electrocatalysis research, Angew. Chem. Int. Ed. 60 (43) (2021) 23051−23067, https://doi.org/10.1002/anie.202110352.
[8] S.Y. Lee, U.J. Kim, J. Chung, H. Nam, H.Y. Jeong, G.H. Han, H. Kim, H.M. Oh, H. Lee, H. Kim, Y.-G. Roh, J. Kim, S.W. Hwang, Y. Park, Y.H. Lee, Large work function modulation of monolayer MoS_2 by ambient gases, ACS Nano 10 (6) (2016) 6100−6107, https://doi.org/10.1021/acsnano.6b01742.
[9] S.M. Song, J.K. Park, O.J. Sul, B.J. Cho, Determination of work function of graphene under a metal electrode and its role in contact resistance, Nano Lett. 12 (8) (2012) 3887−3892, https://doi.org/10.1021/nl300266p.
[10] P. Lindgren, G. Kastlunger, A.A. Peterson, A challenge to the G ~ 0 interpretation of hydrogen evolution, ACS Catal. 10 (1) (2020) 121−128, https://doi.org/10.1021/acscatal.9b02799.
[11] X. Jiang, W. Zhang, G.-R. Xu, J. Lai, L. Wang, Interface engineering of metal nanomaterials enhance the electrocatalytic water splitting and fuel cell performance, Electrochem. Sci. Adv. 2 (3) (2022) e2100066, https://doi.org/10.1002/elsa.202100066.
[12] T. Tang, X. Bai, Z. Wang, J. Guan, Structural engineering of atomic catalysts for electrocatalysis, Chem. Sci. 15 (14) (2024) 5082−5112, https://doi.org/10.1039/D4SC00569D.
[13] N. Cheng, S. Stambula, D. Wang, M.N. Banis, J. Liu, A. Riese, B. Xiao, R. Li, T.-K. Sham, L.-M. Liu, G.A. Botton, X. Sun, Platinum single-atom and cluster catalysis of the hydrogen evolution reaction, Nat. Commun. 7 (1) (2016) 13638, https://doi.org/10.1038/ncomms13638.

[14] C. Li, J.-B. Baek, Recent advances in noble metal (Pt, Ru, and Ir)-Based electrocatalysts for efficient hydrogen evolution reaction, ACS Omega 5 (1) (2020) 31–40, https://doi.org/10.1021/acsomega.9b03550.
[15] G. Gao, L.-W. Wang, A potential and pH inclusive microkinetic model for hydrogen reactions on Pt surface, Chem Catal. 1 (6) (2021) 1331–1345, https://doi.org/10.1016/j.checat.2021.10.006.
[16] O. Peng, Q. Hu, X. Zhou, R. Zhang, Y. Du, M. Li, L. Ma, S. Xi, W. Fu, Z.-X. Xu, C. Cheng, Z. Chen, K.P. Loh, Swinging hydrogen evolution to nitrate reduction activity in molybdenum carbide by ruthenium doping, ACS Catal. 12 (24) (2022) 15045–15055, https://doi.org/10.1021/acscatal.2c04584.
[17] H. Li, X. Han, S. Jiang, L. Zhang, W. Ma, R. Ma, Z. Zhou, Controllable fabrication and structure evolution of hierarchical 1T-MoS_2 nanospheres for efficient hydrogen evolution, Green Energy Environ. 7 (2) (2022) 314–323, https://doi.org/10.1016/j.gee.2020.09.003.
[18] M. Shao, P. Wang, Y. Wang, B. Wang, Y. Wang, J. Xu, Continuous synthesis of few-layer MoS_2 with highly electrocatalytic hydrogen evolution, Green Energy Environ. 6 (6) (2021) 858–865, https://doi.org/10.1016/j.gee.2020.04.008.
[19] Y. Zhang, Y. Kuwahara, K. Mori, C. Louis, H. Yamashita, Hybrid phase 1T/2H-MoS_2 with controllable 1T concentration and its promoted hydrogen evolution reaction, Nanoscale 12 (22) (2020) 11908–11915, https://doi.org/10.1039/D0NR02525A.
[20] K. Zhang, B. Jin, Y. Gao, S. Zhang, H. Shin, H. Zeng, J.H. Park, Aligned heterointerface-induced 1T-MoS_2 monolayer with Near-Ideal Gibbs free for stable hydrogen evolution reaction, Small 15 (8) (2019) 1804903, https://doi.org/10.1002/smll.201804903.
[21] Z. Hong, W. Hong, B. Wang, Q. Cai, X. He, W. Liu, Stable 1T −2H MoS_2 heterostructures for efficient electrocatalytic hydrogen evolution, Chem. Eng. J. 460 (2023) 141858, https://doi.org/10.1016/j.cej.2023.141858.
[22] Z. Kan, B. Jin, Y. Gao, S. Zhang, H. Shin, H. Zeng, J.H. Park, Aligned heterointerface-induced 1T-MoS_2 monolayer with Near-Ideal Gibbs free for stable hydrogen evolution reaction, Small 15 (2019) 1804903, https://doi.org/10.1002/smll.201804903.
[23] G. Li, D. Zhang, Q. Qiao, Y. Yu, D. Peterson, A. Zafar, R. Kumar, S. Curtarolo, F. Hunte, S. Shannon, Y. Zhu, W. Yang, L. Cao, All the catalytic active sites of MoS_2 for hydrogen evolution, J. Am. Chem. Soc. 138 (51) (2016) 16632–16638, https://doi.org/10.1021/jacs.6b05940.
[24] D. Han, N. Gao, J. Ge, C. Liu, W. Xing, Activating MoS_2 via electronic structure modulation and phase engineering for hydrogen evolution reaction, Catal. Commun. 164 (2022) 106427, https://doi.org/10.1016/j.catcom.2022.106427.
[25] N. Solati, C. Karakaya, S. Kaya, Advancing the understanding of the structure–activity–durability relation of 2D MoS_2 for the hydrogen evolution reaction, ACS Catal. 13 (1) (2023) 342–354, https://doi.org/10.1021/acscatal.2c03719.
[26] A. Bala, A. Sen, Y.-H. Kim, Y.-M. Kim, S. Gandla, H. Park, S. Kim, Large-area MoS_2 nanosheets with triangular nanopore arrays as active and robust electrocatalysts for hydrogen evolution, J. Phys. Chem. C 126 (23) (2022) 9696–9703, https://doi.org/10.1021/acs.jpcc.2c01859.
[27] Z. Wan, E.W. Streed, M. Lobino, S. Wang, R.T. Sang, I.S. Cole, D.V. Thiel, Q. Li, Laser-reduced graphene: synthesis, properties, and applications, Adv. Mater. Technol. 3 (4) (2018) 1700315, https://doi.org/10.1002/admt.201700315.
[28] J. Tang, J. Huang, D. Ding, S. Zhang, X. Deng, Research progress of 1T-MoS_2 in electrocatalytic hydrogen evolution, Int. J. Hydrog. Energy 47 (94) (2022) 39771–39795, https://doi.org/10.1016/j.ijhydene.2022.09.162.
[29] Y. Li, H. Wang, L. Xie, Y. Liang, G. Hong, H. Dai, MoS_2 nanoparticles grown on graphene: an advanced catalyst for the hydrogen evolution reaction, J. Am. Chem. Soc. 133 (19) (2011) 7296–7299, https://doi.org/10.1021/ja201269b.
[30] R. Ge, W. Li, J. Huo, T. Liao, N. Cheng, Y. Du, M. Zhu, Y. Li, J. Zhang, Metal-ion bridged high conductive RGO-M-MoS_2 (M = Fe^{3+}, Co^{2+}, Ni^{2+}, Cu^{2+} and Zn^{2+}) composite electrocatalysts for photo-assisted hydrogen evolution, Appl. Catal. B Environ. 246 (2019) 129–139, https://doi.org/10.1016/j.apcatb.2019.01.047.
[31] M. Jin, X. Zhang, S. Niu, Q. Wang, R. Huang, R. Ling, J. Huang, R. Shi, A. Amini, C. Cheng, Strategies for designing high-performance hydrogen evolution reaction electrocatalysts at large current densities above 1000 mA cm^{-2}, ACS Nano 16 (8) (2022) 11577–11597, https://doi.org/10.1021/acsnano.2c02820.
[32] L.-F. Zhang, J. Tang, S.-Y. Liu, O.-W. Peng, R. Shi, B.N. Chandrashekar, Y. Li, X. Li, X.-N. Li, B.-M. Xu, C. Cheng, A laser irradiation synthesis of strongly-coupled VOx-reduced graphene oxide composites as enhanced performance supercapacitor electrodes, Mater. Today Energy 5 (2017) 222–229, https://doi.org/10.1016/j.mtener.2017.07.004.
[33] Q. Huang, X. Li, M. Sun, L. Zhang, C. Song, L. Zhu, P. Chen, Z. Xu, W. Wang, X. Bai, The mechanistic insights into the 2H-1T phase transition of MoS_2 upon alkali metal intercalation: from the study of dynamic sodiation processes of MoS_2 nanosheets, Adv. Mater. Interfaces 4 (15) (2017) 1700171, https://doi.org/10.1002/admi.201700171.
[34] N.P. Kondekar, M.G. Boebinger, E.V. Woods, M.T. McDowell, In Situ XPS investigation of transformations at crystallographically oriented MoS_2 interfaces, ACS Appl. Mater. Interfaces 9 (37) (2017) 32394–32404, https://doi.org/10.1021/acsami.7b10230.
[35] R. Al-Gaashani, A. Najjar, Y. Zakaria, S. Mansour, M.A. Atieh, XPS and structural studies of high quality graphene oxide and reduced graphene oxide prepared by different chemical oxidation methods, Ceram. Int. 45 (11) (2019) 14439–14448, https://doi.org/10.1016/j.ceramint.2019.04.165.
[36] X. Zhang, S. Wang, C.-K. Lee, C.-M. Cheng, J.-C. Lan, X. Li, J. Qiao, X. Tao, Unravelling the effect of sulfur vacancies on the electronic structure of the MoS_2 crystal, Phys. Chem. Chem. Phys. 22 (38) (2020) 21776–21783, https://doi.org/10.1039/C9CP07004D.
[37] S. Goldie, S. Bush, J. Cumming, K. Coleman, A statistical approach to Raman analysis of graphene-related materials: implications for quality control, ACS Appl. Nano Mater. 3 (2020) 11229–11239, https://doi.org/10.1021/acsanm.0c02361.
[38] W. Liu, G. Speranza, Tuning the oxygen content of reduced graphene oxide and effects on its properties, ACS Omega 6 (9) (2021) 6195–6205, https://doi.org/10.1021/acsomega.0c05578.
[39] L.M. Malard, D.L. Mafra, S.K. Doorn, M.A. Pimenta, Resonance Raman scattering in graphene: probing phonons and electrons, Solid State Commun. 149 (27) (2009) 1136–1139, https://doi.org/10.1016/j.ssc.2009.02.045.
[40] C. Kampalapura Swamy, A. Hezam, A. Mavinakere Ramesh, D. Habbanakuppe Ramakrishnegowda, D.K. Purushothama, J. Krishnegowda, R. Kanchugarakoppal S, S. Shivanna, Microwave hydrothermal synthesis of copper induced ZnO/gC_3N_4 heterostructure with efficient photocatalytic degradation through S-scheme mechanism, J. Photochem. Photobiol. Chem. 418 (2021) 113394, https://doi.org/10.1016/j.jphotochem.2021.113394.
[41] A. Kahn, Fermi level, work function and vacuum level, Mater. Horiz. 3 (1) (2016) 7–10, https://doi.org/10.1039/C5MH00160A.
[42] T. Yoon, Q. Wu, D.-J. Yun, S.H. Kim, Y.J. Song, Direct tuning of graphene work function via chemical vapor deposition control, Sci. Rep. 10 (1) (2020) 9870, https://doi.org/10.1038/s41598-020-66893-y.
[43] S. Kikuchi, Y. Takahashi, T. Sakata, Measurement on work function of polycrystalline zinc oxide covered by organic dye, Appl. Opt. 8 (S1) (1969) 42–44, https://doi.org/10.1364/AO.8.S1.000042.
[44] S. Ringe, Approaching in-depth mechanistic understanding of electrochemical hydrogen conversion from computational simulations, Chem Catal. 1 (6) (2021) 1160–1162, https://doi.org/10.1016/j.checat.2021.10.019.